J Sol-Gel Sci Technol (2016) 80:769–782
DOI 10.1007/s10971-016-4155-4

ORIGINAL PAPER: SOL-GEL AND HYBRID MATERIALS FOR CATALYTIC, PHOTOELECTROCHEMICAL AND SENSOR APPLICATIONS

Physico-chemical property-driven dielectric behaviour and catalytic activity of nanocrystalline mullite synthesized from monophasic precursor gel

Arpan Kool[1] · Pradip Thakur[1,2] · Biswajoy Bagchi[1,3] · Nayim Sepay[4] · Sukhen Das[1,5]

Received: 4 May 2016 / Accepted: 12 July 2016 / Published online: 20 July 2016

Abstract Nanocrystalline mullite was synthesized from single-phase mullite precursor with occurrence of mullite phases at 550 °C which is very low compared to traditional mullitization temperatures. Microstructural study showed uniform nanosized grains (20 nm) forming spherical aggregates at lower temperatures with equiaxed grains of mullite formed from the mullite seeds via nucleation and growth at 1400 °C. Frequency-dependent dielectric properties of nanosized mullite have been investigated related to sintering temperature, amount of mullite, porosity and grain size of mullite. The mullite nanocrystals were also an efficient catalyst in Biginelli reaction which is a multi-component assembly process under solvent-free condition.

Graphical Abstract Mechanistic growth of nanocrystalline mullite from a single-phase sol–gel precursor with its physico-chemical property-dependent dielectric behaviour and catalytic activity.

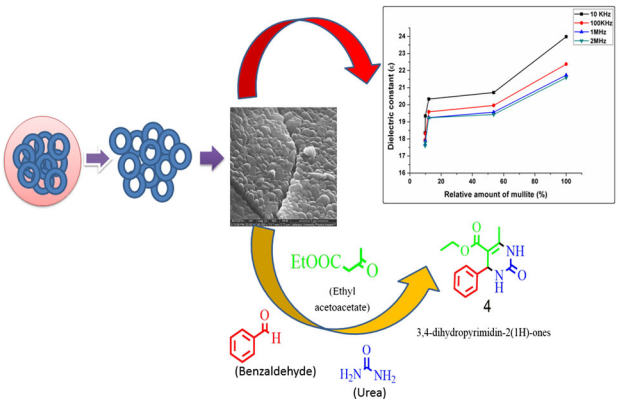

Keywords Mullite · Sol–gel processing · Microstructure · Dielectric properties · Catalysis

1 Introduction

Mullite is an aluminosilicate of chemical formula $Al_2[Al_{2+2x}Si_{2-2x}]O_{10-x}\otimes_x$ with $\otimes$ denoting an oxygen vacancy and average number of oxygen vacancies per unit cell (x) = 0.25 and 0.4 corresponding to stoichiometric and alumina rich mullite, respectively [1]. Mullite, traditionally used as structural ceramics, has recently found emerging scope to be used as functional ceramics acquiring enormous technological importance due to its highly favourable chemical and physical properties such as high-temperature strength [2], excellent creep resistance [3], chemical inertness, low thermal conductivity, low thermal expansion

✉ Sukhen Das
sdasphysics@gmail.com

1 Department of Physics, Jadavpur University, Kolkata 700032, India

2 Department of Physics, Netaji Nagar College for Women, Kolkata 700092, India

3 Fuel Cell and Battery Division, Central Glass and Ceramic Research Institute, Kolkata 700032, India

4 Department of Chemistry, Jadavpur University, Kolkata 700032, India

5 Present Address: Department of Physics, IIEST, Howrah, West Bengal 711103, India

coefficient [4] and good dielectric behaviour [5]. Manifestation of desired physico-chemical properties is closely related to microstructures [6] and other physical properties [7]. Parmentier and Vilminot [8] in their work elaborately discussed the dependence of mullite crystallization on different synthesis procedures and compositions, whereas Okada et al. [9] described ageing temperature-dependent mullitization and Kaya et al. [10] investigated dependence of mullitization behaviour on precursor molecules. Thus, there further remains wide scope to study and follow the mullitization sequences for any synthesis procedure employed to achieve optimum results. A thorough literature survey revealed several methods of mullite synthesis such as thermal decomposition of natural aluminosilicate minerals [11], chemical vapour deposition [12], spray pyrolysis [13], sol–gel technique [14], hydrothermal synthesis [15], spark plasma sintering [16]. Among these, sol–gel processing using different precursor materials containing alumina and silica (generally silicon and aluminium alkoxides) has been a promising technique to fabricate high purity mullite [17]. This is because sol–gel mixing of precursors at molecular level not only ensures highly controllable chemical composition, low-temperature sintering capability and uniform nanometre-sized particles but also is a simple, economic and effective method to produce high-quality ceramic powder.

As demonstrated in the review made by Cividanes et al. [18], sol–gel precursors of mullite have been categorized as single phase or monophasic and diphasic depending on the scale and homogeneity of the mixing between alumina and silica precursors: (1) Type 1 or single-phase or monophasic precursors are characterized by atomic level mixing of Al and Si which lead to mullite formation below 1000 °C without any intermediate spinel phase. In this system, intimate mixing is facilitated by slow hydrolysis of alumina/silica alkoxides or salts [19] and mullitization occurs by three sequential steps: nucleation, growth and coalescence [20] and (2) in case of Type 2 or diphasic precursors, aluminium and silicon in colloidal suspension interact to produce mullite above 1200 °C [21]. Mullite grain growth is controlled by diffusion between alumina/silica particles at the grain interface [22]. Consequently, Zhou et al. [23] showed that diphasic system produce acicular mullite crystals after sintering (diffusion controlled anisotropic growth) while monophasic precursors lead to equiaxed mullite grains.

Nishio and Fujiki [24] first reported that mullite without any mineralizer started to crystallize at relatively low temperature of 600 °C and mullite fibres were formed when heated at 1000 °C. Ban et al. [25] further characterized the low-temperature mullitization by synthesizing mullite using Nishio and Fujiki's method after ageing of gels for several weeks. Effect of different dopants such as metal oxides and metal ions on mullitization behaviour was previously investigated by different researchers. Hong and Messing [26] studied mullite transformation kinetics for P_2O_5, TiO_2 and B_2O_3 doping and Kong et al. [27] investigated the effect of transition metal oxides on mullitization. Further effect of alkaline earth metal oxides, copper oxide, nickel and cobalt ions and V_2O_5 on mullitization was studied by Kong et al. [28], Martisius and Giraitis [29], Bagchi et al. [30] and Roy et al. [31], respectively. From these studies, it can easily be concluded that low-temperature mullitization may be obtained by ions and oxide mineralizers resulting from pronounced Jahn–Teller distortion and lowering of viscosity, whereas mineralizer-free mullitization at lower temperature is very difficult to obtain due to lack of homogeneity. Thus, for the low-temperature processing of mullite ceramics, a homogeneous monophasic or single-phase precursor system is desired.

There are numerous reports regarding the study and mechanism of mullitization from diphasic precursor gels, but fewer works exist describing the complete temperature-dependent study of mineralizer-free mullitization from nucleation stage with associated changes in grain morphology and size at nanoscale regime in monophasic system.

Moreover, understanding the effect of different physico-chemical properties on dielectric behaviour of mullite is not only an area of utter interest but also necessary to achieve desired electrical applications based on mullite ceramics. Although effect of different dopants on the dielectric behaviour of mullite were reported earlier, a very few reports regarding the effect of physico-chemical properties (e.g. grain size and porosity) have yet been published till days. Mullite can be used as high-temperature catalysts due to its high-temperature stability and inertness. However, there was no such report for the use of mullite as chemical catalysts.

In this paper, we have synthesized mullite precursors using aluminium isopropoxide (AIP), aluminium nitrate nonahydrate (ANN) and tetraethyl orthosilicate (TEOS). Since chemical heterogeneity may be formed in the gel due to the higher hydrolysis rate of aluminium alkoxide than that of TEOS, ANN was used in the synthesis to slow down the hydrolysis [14]. A temperature-dependent mullitization was studied in the range of 550–1400 °C followed by detailed characterization of phase formation, microstructure and densification. X-ray diffraction (XRD), Fourier transform infrared spectroscopy (FTIR) and field emission scanning electron microscopy (FESEM) study revealed mullitization at a very low temperature (550 °C) and then growth from spherical granules to nanometre-sized dense equiaxed grains at 1400 °C. The influence of different physico-chemical properties (e.g., sintering temperature, porosity, bulk density, amount of mullite, grain size) on the

dielectric parameters of nanocrystalline mullite without any mineralizer was analysed, and we report herein that mullite nanocrystals can catalyse Biginelli reaction for the condensation of aldehyde, urea and an active methylene compound under solvent-free conditions.

2 Experimental

2.1 Materials

The chemicals used in this study are aluminium nitrate nonahydrate ($Al(NO_3)_3{\cdot}9H_2O$) (ANN) (Merck, Worli, Mumbai, India), aluminium isopropoxide ($Al(O\text{-}i\text{-}Pr)_3$) (AIP) (Loba Chemie) and tetraethyl orthosilicate (TEOS) ($Si(OC_2H_5)_4$) (Merck, Honenbrunn, Germany). All the chemicals are 99 % pure. Double-distilled water is used throughout the synthesis.

2.2 Sol–gel synthesis of nanocrystalline mullite

Figure 1 shows a scheme for the synthesis procedure of mullite precursor. Precursor gel was synthesized by using ANN and AIP as alumina sources and TEOS as silica source. Stoichiometric amount of AIP and TEOS was added simultaneously to 0.5(M) ANN solution in double-distilled water under stirring condition at room temperature. Molar ratio of AIP to that of ANN was maintained at 3.5 in order to maintain homogeneity and better spinnability of the sol to initiate low-temperature mullitization [14]. Mole ratio of alumina and silica was kept at 1.5 and pH of the solution was ~5. This sol was kept under uninterrupted stirring at 350 rpm for 12 days until gelation. The gel was dried in a hot air oven at 250 °C for 6 h and then finely ground in an agate mortar and pestle. The free flowing powder was made in form of pellets using a hydraulic press of average diameter 13 mm and thickness 2 mm under a pressure of 100 psi. powder The powder was then sintered in air atmosphere (in both pellet and powder form) at the temperatures regime of 550–1400 °C with a heating rate of 3 °C/min and 4 h soaking to study mullitization sequences.

2.3 Characterizations

Thermal analysis of the precursor gel was done using simultaneous differential thermal analysis and thermogravimetric analysis (DTA-TG) (DTG-60H, Shimadzu ((Asia Pacific) Pte. Ltd., Singapore) under N_2 atmosphere within the temperature range from ambient to 1000 °C with an increment of 10 °C/min.

Crystallization, phase formation and microstructure of mullite particles were followed by X-ray diffraction (XRD)

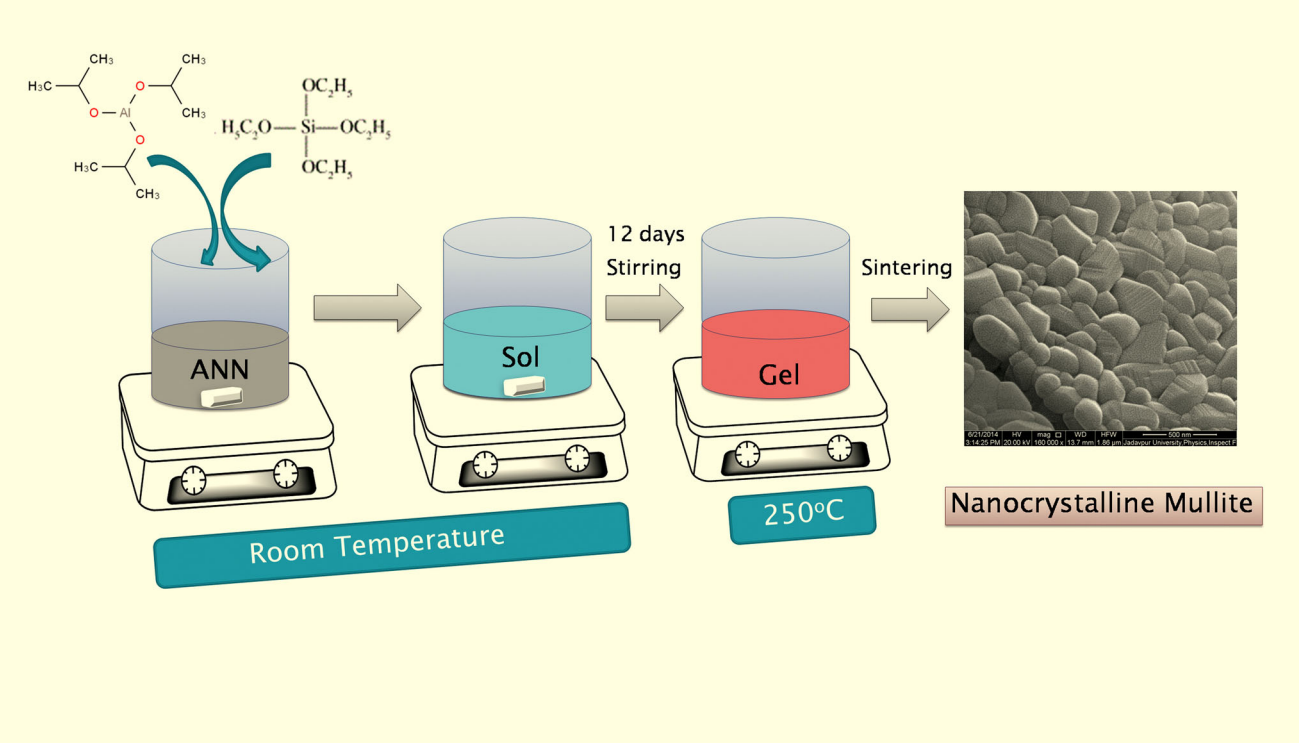

Fig. 1 A schematic diagram for the synthesis of mullite nanocrystals

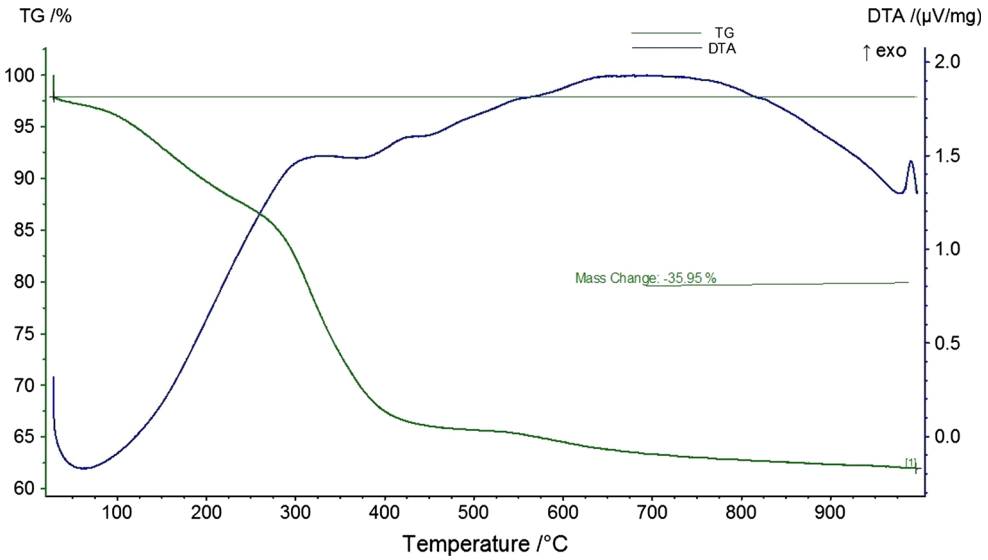

Fig. 2 DTA-TG curve of mullite precursor gel dried at 250 °C (M250)

(Bruker AXS INC., Madison, WI), Fourier transform infrared spectroscopy (FTIR—8400S, Shimadzu) and FESEM (INSPECT F50, Netherland). The crystal structure development of the mullite was studied by the X-ray diffraction using Cu Kα radiation ~1.54 Å, 2θ = 10°–70°, scan speed 0.3 s/step, increment—0.02, operating voltage—40 kV and operating current—40 mA.

FTIR spectroscopic studies of mullite powders sintered at different temperatures were done by KBr pellet method between the wavenumbers 400–1250 cm^{-1} for identification of characteristic bonds in mullite structure.

Relative density of the samples was determined by using displacement method according to Archimedes' principle. The density of the sample is $\rho = m/V$, where m is the mass of the sample and V is the volume as determined by the displacement method. Taking theoretical density of mullite as 3.16 g/cc, the relative density $(\frac{\text{Calculated density}}{\text{Theoritical density}}) \times 100\,\%)$ and apparent porosity of the mullite samples sintered at different temperatures was measured.

The frequency dependence of capacitance and tan δ of the samples were studied using a digital LCR meter (Agilent, E4980A) with circular Ag electrodes at room temperature and pressure. 1 V signal was applied in the frequency range between 20 Hz and 2 MHz. The dielectric constant (ε) and the ac conductivity (σ_{ac}) of the samples were calculated using following equations.

$$\varepsilon = C \cdot d/\varepsilon_0 A \quad \text{and} \quad \sigma_{ac} = 2\pi f \varepsilon_0 \varepsilon \tan\delta$$

where, C, d, A and tan δ are the capacitance, thickness, area and tangent loss of the samples, respectively, and f is the frequency in Hz applied across the samples and ε_0 is permittivity of free space with value 8.854×10^{-12} F/m.

The catalytic activity of nanocrystalline mullite was observed in Biginelli reaction for the condensation of benzaldehyde, urea and ethyl acetoacetate compound under solvent-free conditions, and the structure of the product was confirmed by Bruker's 300, 300 MHz NMR spectrometer using $CDCl_3$ solution.

3 Results and discussion

3.1 DTA-TG analysis of gel

The endothermic peaks at lower temperatures in the DTA curve (Fig. 2) correspond to the removal of structural water, isopropyl alcohol, NO_2, etc. with corresponding weight losses.

The characteristic exothermic peak of mullite transformation was found in the DTA graph near 988 °C. Moreover, no recognizable mass loss was found in the TG curve which is indicative of the presence of mullite.

3.2 X-ray diffraction analysis

In order to study the growth and crystallization of mullite phase, the gel was sintered from 550 to 1400 °C. In the XRD pattern (Fig. 3), no crystalline mullite phase was observed in case of dried gel at 250 °C (M 250). However, the amorphous part present in the dried gel was found to convert into mullite when sintered at 550 °C and higher (M550—M1400), which was evident from the characteristic reflections in XRD spectra. Thus, it can be concluded that mullitization commenced at 550 °C (with very low crystallinity) though the exothermic peak corresponding to

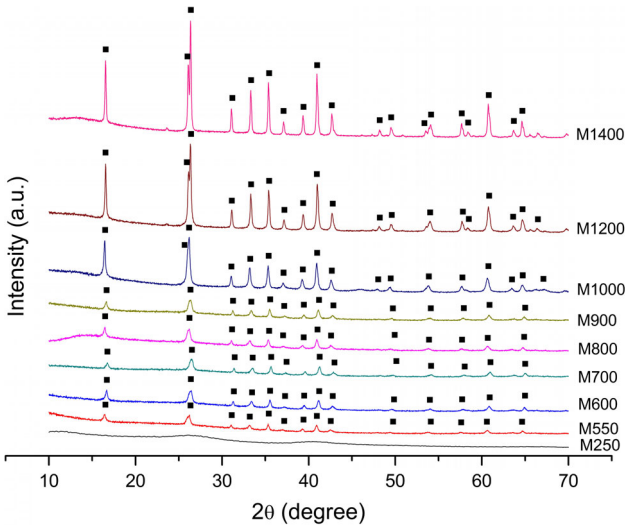

Fig. 3 Comparative X-ray diffraction pattern of precursor mullite gel sintered at different temperatures (M250, M550, M600, M700, M800, M900, M1000, M1200, M1400, *filled square* mullite)

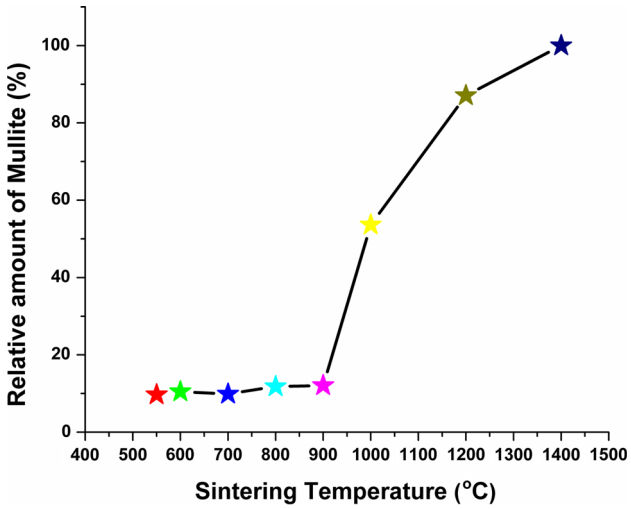

Fig. 4 Formation curve of mullite with increasing temperatures

the formation of mullite was obtained near 988 °C in DTA thermogram which can occur due to the dynamic nature of DTA analysis for which it cannot detect minute heat changes associated with partial crystallizations occurring below 980 °C [32]. The relative amount of mullite crystallization was measured by calculating the peak height of $2\theta = 16°$ assuming 100 % mullitization obtained at 1400 °C and found to remain almost constant in the temperature range of 550–900 °C but steeply increased above 1000 °C reaching almost completion at 1400 °C (Fig. 4).

It can also be observed that characteristic peak of mullite at $2\theta = 26°$ forms a doublet above 1000 °C indicating transformation from t-mullite into o-mullite [18]. Thus, with increase in temperature both the amount and crystallinity of mullitization were found to increase. Average crystallite size from XRD data was calculated and is enumerated in Table 1 using Scherrer's equation:

$$D = \frac{0.9\lambda}{\beta\cos\theta} \quad (1)$$

where D is the average diameter, λ is the wavelength of CuKα line, β is full width of half maxima (FWHM) in radian and θ is Bragg's angle.

The crystallite dimension was found not to vary distinctly for the temperature range of 550–900 °C, but beyond 1000 °C, the size increased due to the enhanced grain growth. The average crystallite dimension as calculated from Scherrer's equation for the lower temperature sintering was found to reside in the range of 32–38 nm, whereas at 1000 °C the size became ~45 nm and increased up to 57 nm at 1400 °C.

The broadening in the X-ray diffraction lines for the crystallites below 100 nm can be due to both the particle size and strain neglecting instrumental effect [33]. The broadening (β_r) due to small particle size and lattice strain may be represented as:

$$\beta_r = \beta_c + \beta_s = \frac{0.9\lambda}{D\cos\theta} + \varepsilon\tan\theta$$

where broadening due to small particles size can be expressed as $\beta_c = \frac{0.9\lambda}{D\cos\theta}$ and broadening due to lattice strain was expressed by the relation: $\beta_s = \varepsilon\tan\theta$. Here, ε the strain distribution within the material and θ the Bragg angle.

$$\beta_r \cos\theta = \frac{0.9\lambda}{D} + \varepsilon\sin\theta$$

With the help of this equation, lattice strains of the mullite at different sintering temperatures were calculated from the slopes of the plot between $\beta_r\cos\theta$ and sin θ (Fig. 5a).

The lattice strain was found to decrease from 550 to 600 °C sintering and then the value increased up to 800 °C (Table 1). Mullitization initiated at 550 °C with the distinct growth of mullite being started from 600 °C. Thereafter, moving from 550 to 600 °C, the mullite particles became elongated and agglomerated to form large clusters; hence, a drop in crystal lattice strain resulted from the evolution of formation energy prior to growth. A sudden drop in the strain value was observed at 900 °C, and then, it goes on increasing above 1000 °C (Fig. 5b). The drop in the strain value at 900 °C can be attributed to the transformation of amorphous aluminosilicate into well-crystallized bulk mullite phase around that temperature. This was reflected by the exothermic peak at 980 °C in DTA curve which is indicative of the release in lattice energy during crystallization.

Table 1 Average particle size (from Debye–Scherrer's equation and FESEM micrographs), lattice strain, relative density and apparent porosity with increasing sintering temperatures

Sintering temperature (°C)	Average particle diameter (nm) from Debye–Scherrer's equation	Average particle size (nm) from FESEM micrograph	Crystal strain (%)	Relative density (%)	Porosity from Archimedes' principle (%)
550	38	20	1.254	45	55
600	36	30	1.098	47	53
700	32	45	1.227	48	52
800	36	45	1.343	50	50
900	32	75	0.478	52	48
1000	45	90	0.984	55	45
1200	57	130	1.051	56	44
1400	57	200	1.346	58	42

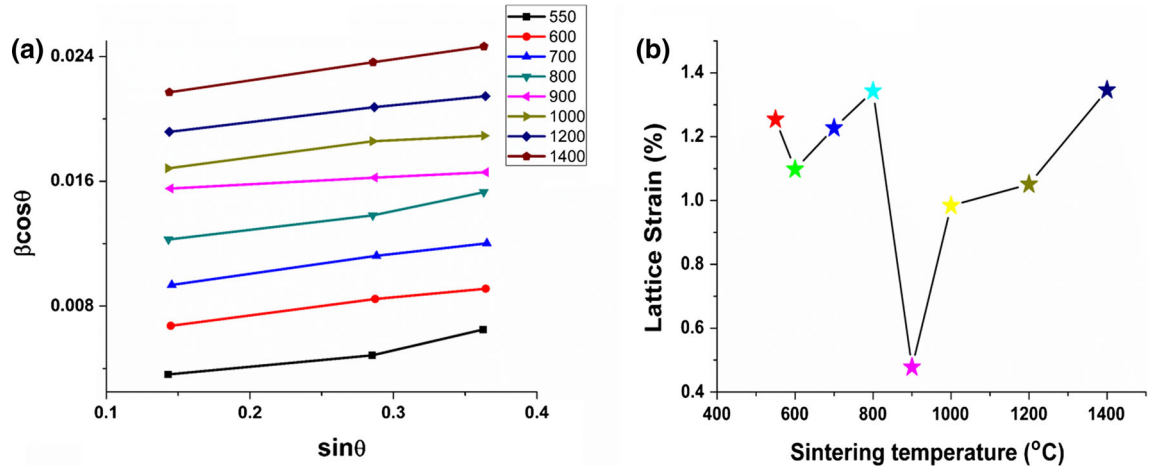

Fig. 5 **a** βcosθ versus sinθ plot of M550–M1400, **b** variation in lattice strain with sintering temperatures

3.3 Fourier transform infrared spectroscopy

A comparative FTIR spectral study of different samples is shown in Fig. 6. In the spectra of 250 °C dried mullite gel (Fig. 6 inset), both Al–O–Al and Si–O–Si vibrations were found around 770 and 465 cm^{-1}. Moreover, Al–O stretching vibration and Al–O–Si vibrations reflected at 905 and 1080 cm^{-1} which indicates homogeneous monophasic nature of the precursor sol [34]. In the comparative spectra, the above-mentioned transmission bands are not prominent due to more intense bands of mullite sintered at higher temperatures. As sintering temperature increased gradually from 550 °C, characteristic vibrations corresponding to mullite started to appear at 510, 586, 730, 841, 1134 and 1165 cm^{-1} in the spectra indicating mullite phase tranformation. Peaks at 510 cm^{-1} correspond to vibration of Al–O stretching as previously indicated by Kool et al. [35], and 586 cm^{-1} is assigned to AlO_6 octahedra as described by Padmaja et al. [34]. Band at 730 cm^{-1} and the wide band below 970 cm^{-1} indicate the vibration mode of AlO_4 tetrahedra and Al–O stretching vibration [36]. The band at 841 cm^{-1} assigned to Si–OH vibration [34] and Si–O stretching mode frequencies were found at 1134 and 1165 cm^{-1} [37]. At sintering temperatures above 1000 °C, bands due to AlO_4 and Si–OH intensified and shifted to 716 and 824 cm^{-1}, respectively, indicating enhanced mullitization.

3.4 FESEM analysis

Morphological characteristics of the mullite nanocrystals were studied using scanning electron microscopy. Sample pellets were sintered from 550 to 1400 °C, and growth of the grains was followed from the scanning electron microscopic images. Extremely fine spherical nanosized particles of the order of 20 nm is distributed throughout the matrix in the micrograph of mullite sintered at 550 °C (Fig. 7a). At 600 °C (Fig. 7b), the particles became

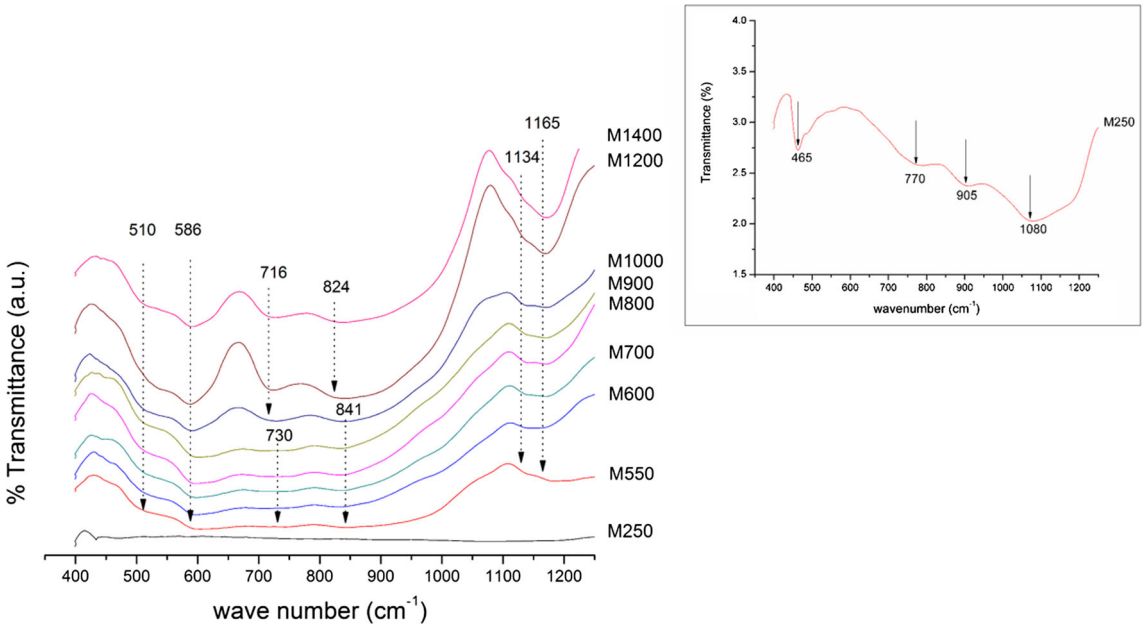

Fig. 6 Comparative FTIR spectra of precursor mullite gel sintered at different temperatures (M250–M1400) (*inset*: FTIR spectrum of mullite precursor gel dried at 250 °C)

somewhat elongated and formed large clusters indicating agglomeration and growth. Similar morphology was observed at 700 °C, 800 °C (Fig. 7c, d) with grains becoming more distinct. Thus, nucleation being initiated in the range of 550–600 °C proceeded to a slow growth process to form larger mullite grains. From 900 to 1200 °C, well-crystallized mullite crystals started to appear at the amorphous–crystal boundary (Fig. 8a–c) with particle size increased to 75 nm possessing oblong morphology. Finally at 1400 °C, uniform mullite grains can be observed with relatively higher density (Fig. 8d). Grain size was in the range of 100–250 nm with both spherical and oblong shaped morphology. It has to be noted that at all sintering temperatures the grain sizes were in the nanoscale dimension which is a consequence of atomic mixing of precursor materials.

3.5 Densification and apparent porosity

Figure 9 represents the variation in relative density and apparent porosity with sintering temperature. Relative density of the samples increased nonlinearly with sintering temperature though densification of mullite was not very high (∼58 %) even after sintering at 1400 °C. This lower density may be attributed to lower segregation of phase and low packing among atoms [38]. Moreover, nanocrystalline dimension of mullite grains (100–250 nm) leads to the formation of local networks which act as barrier to densification [5]. The porosity of the samples showed expected behaviour with around 35 % porosity at 1400 °C.

3.6 Mechanism of mullitization

Sol–gel synthesis of mullite from alkoxide precursors involves hydrolysis and polycondensation of $Al(OH)_3$/$Al(OH)_4$ and $Si(OH)_4$ moieties to form a three-dimensional gel network consisting of Al–O–Al, Si–O–Si and Al–O–Si linkages. This is followed by direct transformation of the precursor gel to mullite at 1000 °C. It is reported that slow hydrolysis of alkoxide precursors give rise to monophasic and nanosized mullite grains. In the present case, slow hydrolysis rate have been achieved by addition of ANN to the alkoxide precursors. During sintering, transitional alumina from AIP and ANN reacts with silica to start nucleation at 550 °C followed by minimal grain growth at higher temperatures. This low-temperature nucleation and small grain size is achieved as a consequence of intimate homogenization and longer gelation period (12 days) of the precursors. A schematic for the reaction mechanism is illustrated in Fig. 10. Thus, the reaction follows a pattern typical of monophasic gel with nanosized mullite crystals formation taking place from a very low temperature.

The different physico-chemical properties (e.g., crystallite diameter, relative density, apparent porosity and crystal strain) with rise in sintering temperatures are enumerated in Table 1.

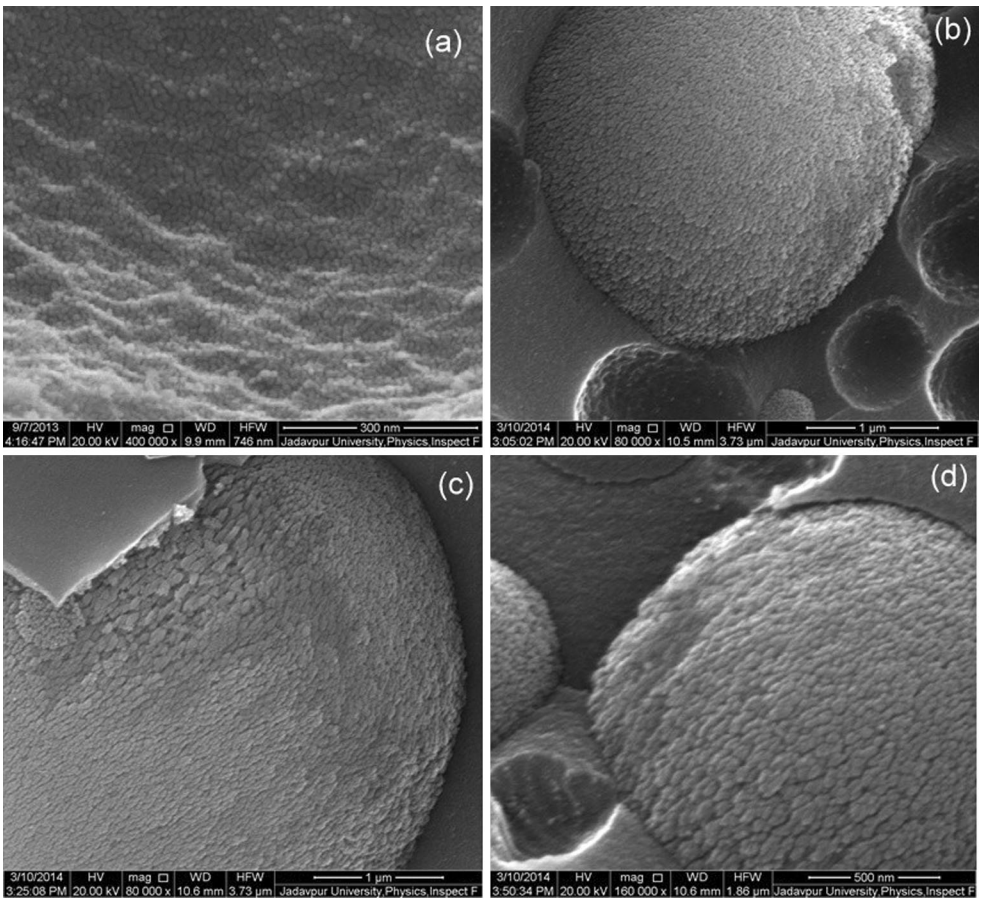

Fig. 7 FESEM micrograph of **a** M550, **b** M600, **c** M700 and **d** M800

3.7 Dielectric properties

3.7.1 Physico-chemical property-dependent dielectric behaviour

Figure 11a shows the dielectric constant and tangent loss at 100 kHz frequency of source as a function of sintering temperature. The dielectric constant increased almost linearly with sintering temperature, and the value of the dielectric constant of mullite was found to be ~22 at 1400 °C sintering temperature which is much higher than that of the traditional ones (~7). The enhanced value of dielectric constant may be due to the entrapped air in the mullite composite with greater porosity relative to conventional mullite (Table 1). Highly porous mullite easily absorbs ambient air containing moisture and the trapped moisture acts cooperatively to enhance the ionic part of the dielectric constant, thus resulting in a total increase in dielectric constant. Tangent losses of nanocrystalline mullite increased as sintering temperature increased from 550 to 700 °C. After further sintering at 900 and 1000 °C, the decrease in tangent loss could be interpreted as the initiated phase transformation from t-mullite to o-mullite at that temperature region which in turn results in lower leak current and thus an effective decrease in tangent loss [39]. With further sintering at 1400 °C, the loss further increased may be due to the enhanced formation of o-mullite. As formation of stable orthorhombic mullite occurs between 900 and 1000 °C from metastable tetragonal mullite, there may be a drop in leak current which decreases tangent loss. Further while o-mullite phase grows rapidly at higher sintering temperature, the increase in tangent loss can be attributed to the higher ionic conductivity of o-mullite and the higher grain boundary conductivity of larger grains that contributes to larger leak current and thus enhanced loss tangent. The variation in dielectric constants and tangent losses at different frequencies are depicted in Fig. 11b, c.

The variations in dielectric constant with relative amount of mullite, average grain size, relative density and apparent porosity at different frequencies are shown in Fig. 12. With increasing amount of well-grown insulating mullite and grain size of the mullite nanocrystals, the

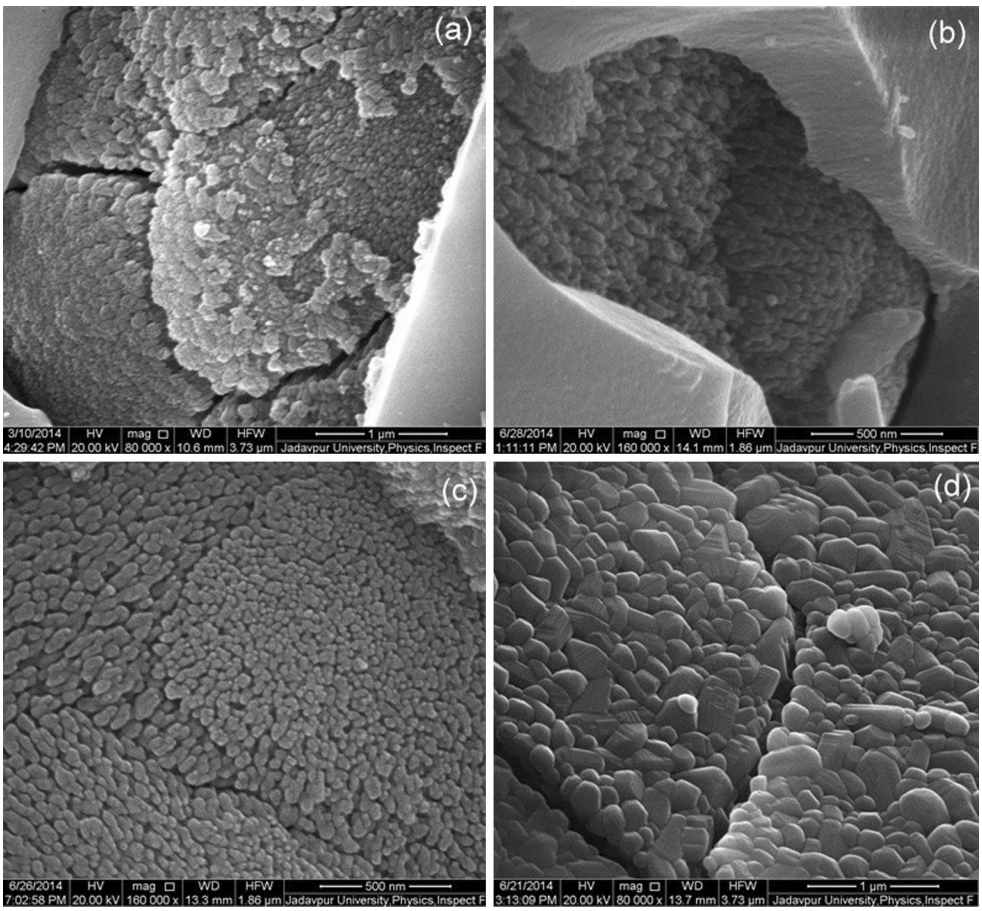

Fig. 8 FESEM micrograph of **a** M900, **b** M1000, **c** M1200 and **d** M1400

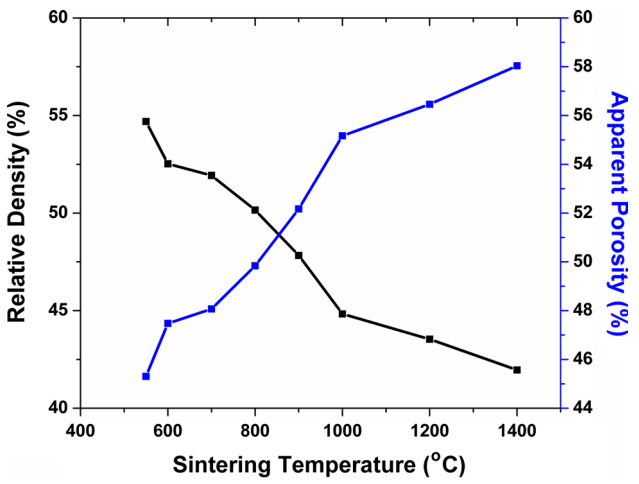

Fig. 9 Variation in relative density and apparent porosity with sintering temperature

enhancement of dielectric constant may be due to improvement in average polarization and the coupling between grains per unit volume as well as greater charge accumulation on larger crystallites of mullite (Fig. 12a, b). As mullite nanocrystal grows, the charge storage on the larger available grain boundaries becomes dominant over the contribution of entrapped moist air. Thus, the dielectric constant increases with amount of mullite though porosity decreases reducing the probability of moist air entrapment. The dielectric properties of materials describe electrical energy storage, dissipation and energy transfer as a result of dielectric polarization which causes charge displacement or rearrangement of molecular dipoles. Therefore, materials with optimized dielectric properties are better suited in energy storage and energy transfer devices (high dielectric) for electronic industries as well as in applications of substrate and packaging materials (low dielectric). The energy and charge storage in the dense matrix of mullite with lesser interconnecting pores is assumed to be higher than that in case of lower dense ones which in turn results in a larger dielectric constant of mullite at higher relative density and lower apparent porosity (Fig. 12c, d). With comparatively better density, larger grain boundaries are available for charge storage; thus, the induced charges on the larger grains and grain boundaries of mullite enhance the dielectric constant.

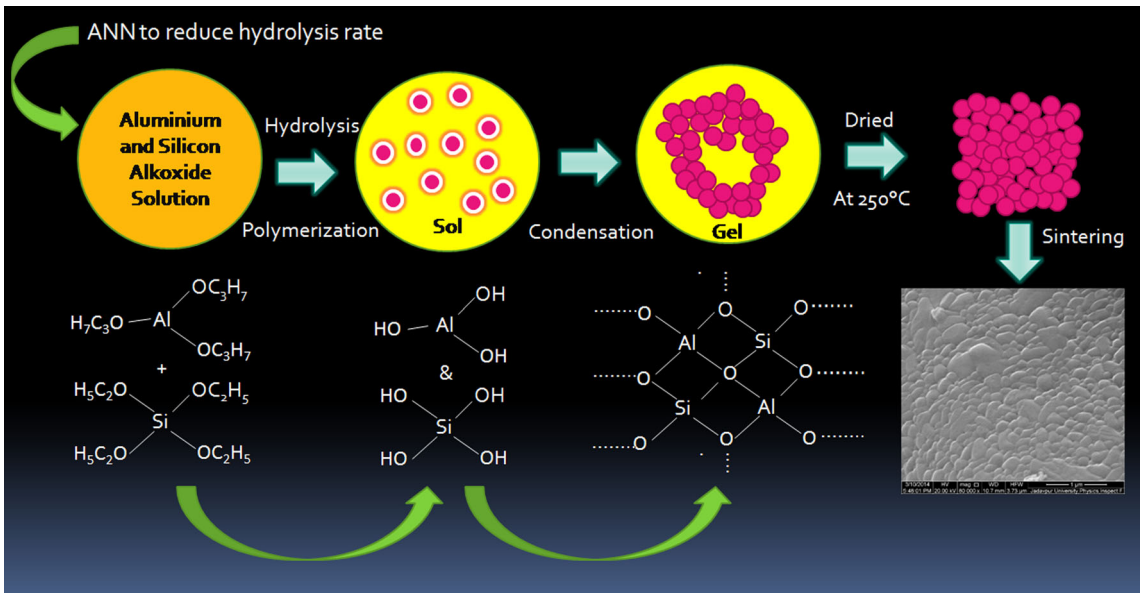

Fig. 10 Mechanistic diagram for the synthesis of equiaxed mullite grains

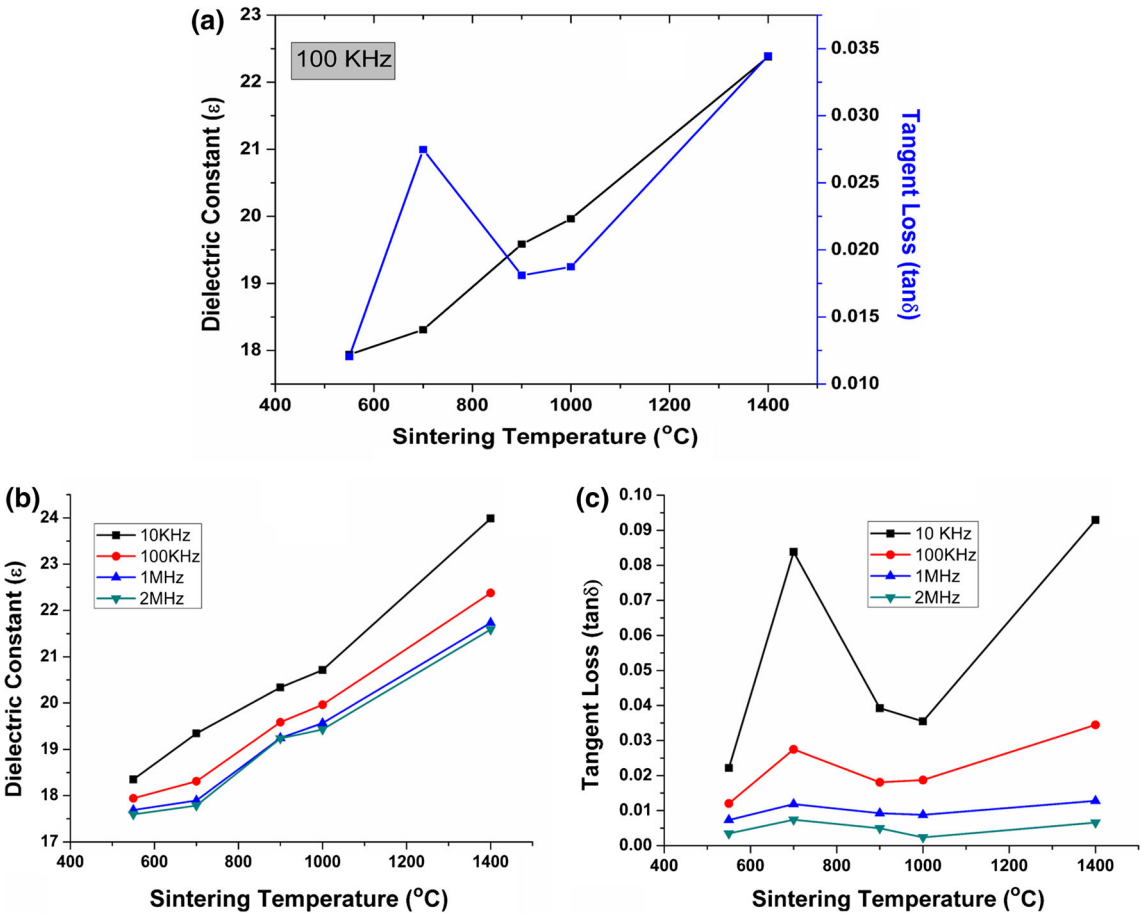

Fig. 11 **a** Dependence of dielectric constant and tangent loss on sintering temperature at 100 kHz, variation in **b** dielectric constant and **c** tangent loss with sintering temperatures at different frequencies

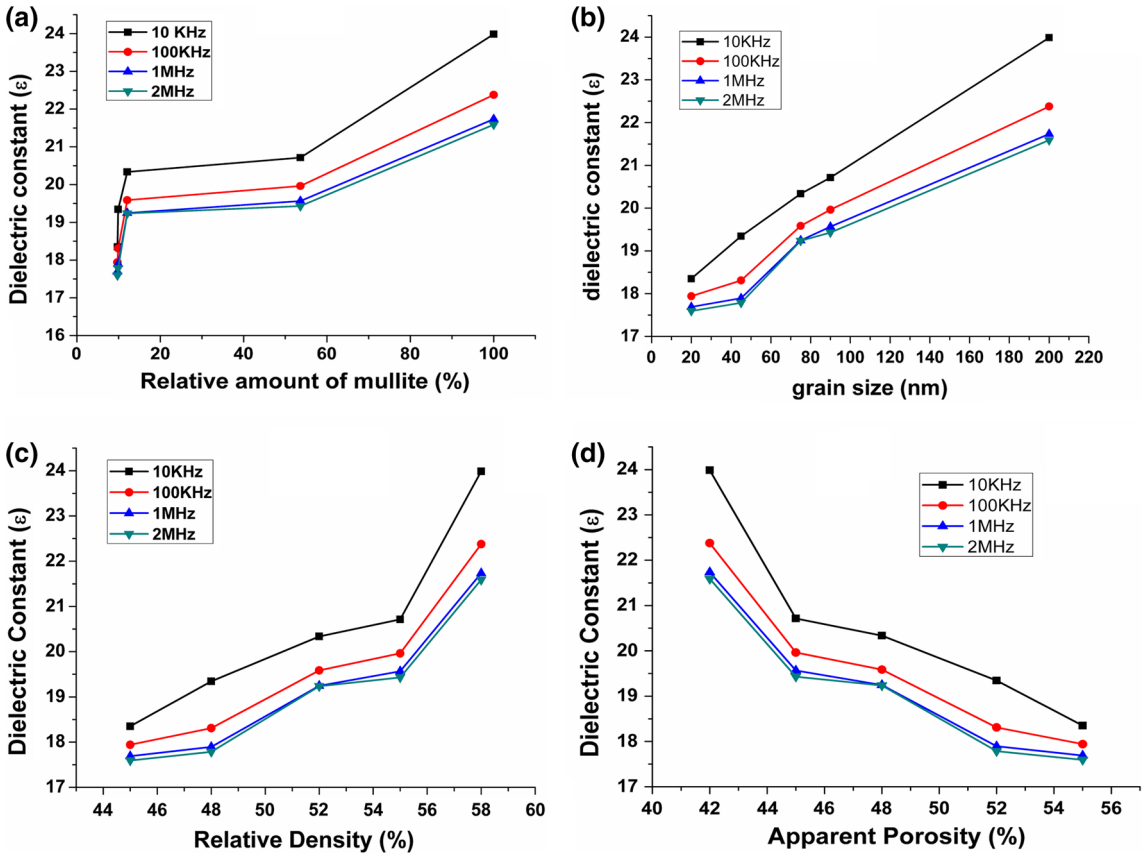

Fig. 12 Dependence of dielectric constant on **a** relative amount of mullite, **b** grain size of mullite, **c** relative density and **d** apparent porosity

3.7.2 Frequency dependence of dielectric behaviour

Figure 13 shows frequency-dependent dielectric properties of nanocrystalline mullite at room temperature and atmospheric pressure. The dielectric constant of mullite decreased with the increase in frequency for all sintering temperatures (Fig. 13a) and saturated at higher frequencies due to restricted movement of induced dipoles which cannot follow the fast rate of polarity change at higher frequency of applied signal. The dominant conduction mechanism in mullite ceramics among Poole–Frenkel, Schottky, ionic hopping and space charge limited current mechanisms are the ionic conduction mechanism via electron hopping between oxygen vacancies [40, 41]. The dielectric constant at lower frequencies can be attributed to different types of polarizations namely atomic, electronic, ionic and interfacial polarizations, whereas behaviours of dielectric constant at higher frequencies is due to the contribution of electronic polarization only. The electronic polarizations can orient themselves with the electric field at the lower frequency range, but at higher frequency, the dipole response is limited with applied voltage since the movement of contributing dipoles is seized. According to Kool et al. [41], the interwell hopping contributes for the dielectric relaxation at lower frequencies resulting in a higher dielectric constant, whereas the dielectric constants of all samples remain almost unaltered at high frequency range because beyond a particular frequency short-range intrawell hopping dominates and the charge carriers do not acquire enough time for long-range interwell hopping before the reversal of the external field. Therefore, with increasing frequency average polarization decreases generating from limited dielectric response that results in a lowering of dielectric constant at higher signal frequency. The gradual increase in overall dielectric constant was already discussed in the previous section.

Figure 13b shows the frequency dependence of tangent loss (tan δ) in nanocrystalline mullite. Electrical energy dissipation or loss in the sample arises from electrical charge transport, dielectric relaxation, resonant transitions and nonlinear dielectric effects. The tan δ is the energy dissipation in dielectrics, which is equal to the ratio of the imaginary part of dielectric constant to the real part and is largely dependent on random grain orientations and grain boundaries too. In low-frequency region, tan δ for all mullite samples are large and gradually decreased with rise

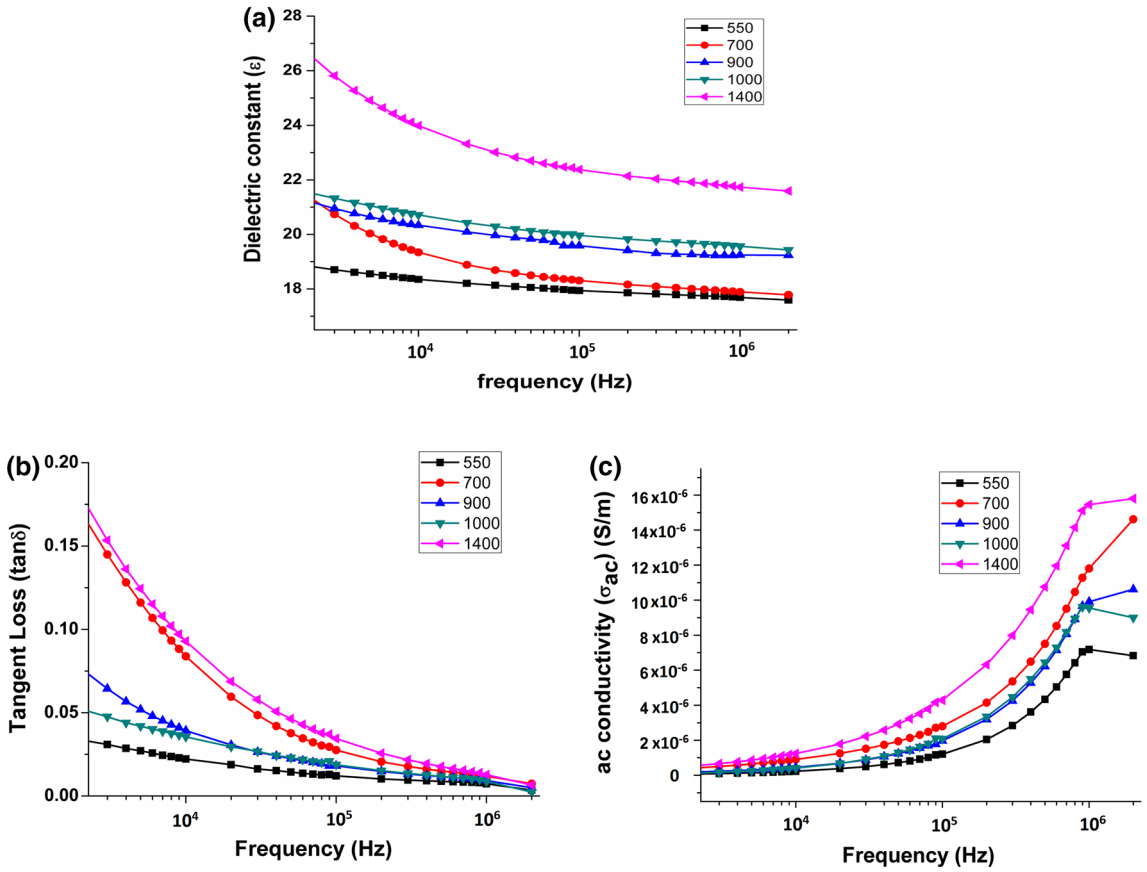

Fig. 13 Frequency dependence of **a** dielectric constant, **b** tangent loss and **c** ac conductivity

in frequencies and attained a saturated value. The induced dielectric polarizations can easily orient themselves with external electric field of lower frequencies and at higher frequencies the lower tangent loss can be attributed to limited dipole responses.

The frequency dependence of ac conductivity (σ_{ac}) of mullite is shown in Fig. 13c. The conductivity of mullite samples can be divided into one low-frequency region which is primarily dominated by dc conductivity and another high-frequency region which is characteristics of frequency-dependent conductivity (Eq. 2).

$$\sigma(\omega) = \sigma_{dc} + \sigma_0 \omega^S \quad (2)$$

where σ_{dc} is the frequency-independent dc conductivity, σ_0 is a temperature-dependent parameter and S lies between 0 and 1. The ac conductivity of the mullite sample increased exponentially with increasing frequency as reflected from the exponential nature of the curve shown in Fig. 13c. This is may be due to the lower mobility of induced dipoles at higher frequencies. Moreover, the sintering temperature dependence of ac conductivity was almost similar to that of tan δ.

3.8 Catalytic activity

Nanocrystalline mullite derived from monophasic sol–gel precursor behaves as an efficient catalyst in Biginelli reaction to synthesize 3,4-dihydropyrimidin-2(1H)-ones (***4***) under solvent-free condition (Fig. 14a). In this reaction, benzaldehyde (***1***), urea (***2***) and ethyl acetoacetate (***3***) condense to the compound ***(4)*** (3,4-dihydropyrimidin-2(1H)-ones) at 80 °C under solvent-free condition with the help of nanocrystalline mullite as catalyst. During the substitution of Si^{4+} sites by Al^{3+}, oxygen-related vacancies are formed along with rearrangement and disordering of tetrahedral cations. Mullite nanocrystals due to these oxygen vacancies may produce lewis acid site which can activate aldehyde and the reaction proceed in the pathway shown in Fig. 14b. The structure of the final product (using mullite sintered at 1400 °C as catalyst) has been confirmed from nuclear magnetic resonance (NMR) spectra (Fig. 14c). In addition, the improved yield of the product ***(4)*** results for mullite sintered at higher temperatures (1000 and 1400 °C) since amount of mullite crystallinity increases with sintering temperature and pronounced oxygen vacancies are

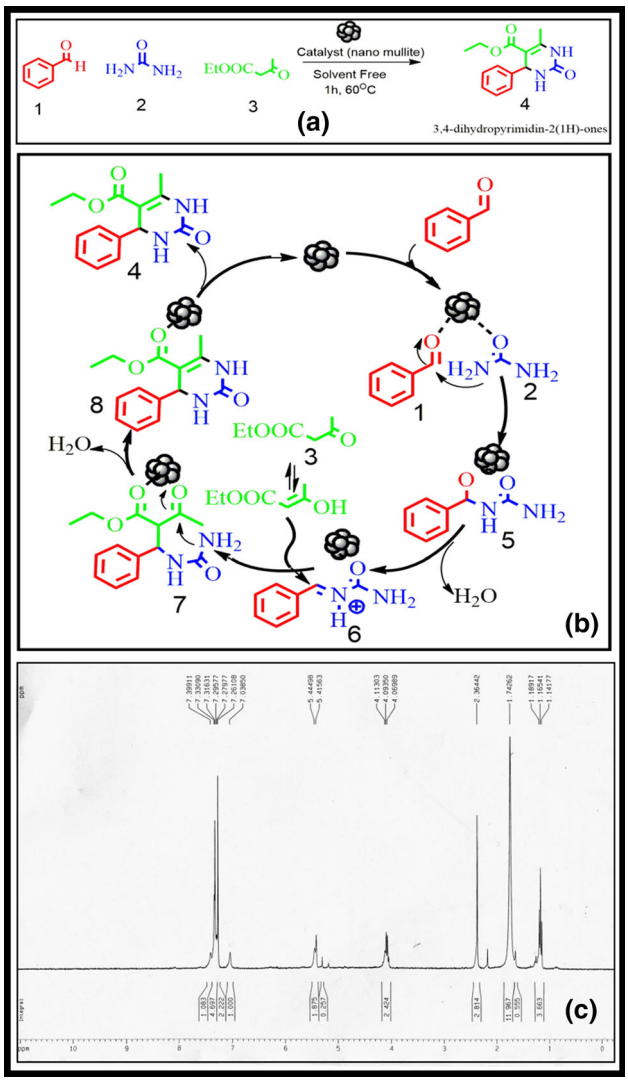

Fig. 14 **a** One-step reaction route using nanocrystalline as catalyst, **b** schematic pathway of catalytic Biginelli reaction under solvent-free condition, **c** NMR spectra of the product using M1400 as catalyst

Table 2 Yield of 3,4-dihydropyrimidin-2(1H)-ones using nanocrystalline mullite catalyst sintered at different temperatures

Sintering temperature (°C)	Time of reaction (h)	Catalytic load (mol%)	Yield of product (%)
550	1	5	65
700	1	5	70
1000	1	5	72
1400	1	5	78

produced (Table 2). Another green aspect of the reaction is the recyclability of the heterogeneous catalyst. The mullite samples can be used as catalyst seven times without any major loss in catalytic activity. Moreover, mullite can be easily separated from the reaction mixture by simple filtration method and can be made organic material-free with dichloromethane washing which make its use more suitable as catalyst in chemical reactions. Thus, mullite can be a better and cheaper catalyst with adequate yield (~65–78 %) and better recyclability as compared to other well-known catalysts such as hydrated iron or nickel chloride or carboxylic acid.

4 Conclusions

In summary, mullite nanocrystals have been synthesized by sol–gel technique from a single-phase gel precursor. Nucleation and growth of mullite crystals have been investigated and characterized by different instrumental techniques. The results (from XRD, FTIR, FESEM) showed that nanosized mullite grains (20 nm) nucleated from precursors at a very low temperature of 550 °C. With increasing temperature grain growth significantly increased after sintering at 900 °C indicating enhanced mullitization. It is interesting to observe that grain size remained in the nanoregime (20–250 nm) at all sintering temperatures (from 550 to 1400 °C) with predominantly spherical and ovoid shaped morphology. This is also evident from the low densification (35 % porosity) behaviour observed at 1400 °C. Thus, the observed morphology and growth kinetics reflects superior homogeneity in the precursors and consequent low-temperature mullitization unseen in other conventional techniques. The dielectric constant of the nanocomposite was found to be larger compared to the traditional ones due to the entrapped air resulting from higher porosity. The dielectric constant of mullite without any dopant was obtained to be ~22 resulting from the definite porosity of mullite nanocrystals and is found to be superior to the reported ones. Study about the effect of other physico-chemical properties on the dielectric behaviour of sol–gel-derived nanocrystalline mullite and its catalytic activity in a multicomponent assembly process with great efficiency reveals the wide scope of nanocrystalline mullite ceramics in both electrical and catalytic applications.

Acknowledgments We are grateful to DST [INSPIRE PROGRAM (No.: DST/INSPIRE Fellowship/2013/797, Code: IF130870)], Government of India, for their financial support.

References

1. Ruscher CH, Schrader G, Gotte M (1996) Infrared spectroscopic investigation in the mullite field of composition: $Al_2(Al_{2+2x}Si_{2-2x})O_{10-x}$ with $0.55 > x > 0.25$. J Eur Ceram Soc 16:169–175
2. Torrecillas R, Fantozzi G, de Aza S, Moya JS (1997) Thermomechanical behaviour of mullite. Acta Mater 45:897–906

3. Torrecillas R, Calderon JM, Moya JS, Reece MJ, Davies CKL, Olagnon C, Fantozzi G (1999) Suitability of mullite for high temperature applications. J Eur Ceram Soc 19:2519–2527
4. Camerucci MA, Urretavizcaya G, Castro MS, Cavalieri AL (2001) Electrical properties and thermal expansion of cordierite and cordierite-mullite materials. J Eur Ceram Soc 21:2917–2923
5. Sanad MMS, Rashad MM, Abdel-Aal EA, El-Shahat MF (2013) Mechanical, morphological and dielectric properties of sintered mullite ceramics at two different heating rates prepared from alkaline monophasic salts. Ceram Int 39:1547–1555
6. de Sola ER, Estevan F, Torres FJ, Alarcón J (2005) Effect of thermal treatment on the structural evolution of 3:2 and 2:1 mullite monophasic gels. J Non-Cryst Solids 351:1202–1209
7. de Sola ER, Torres FJ, Alarcón J (2006) Thermal evolution and structural study of 2:1 mullite from monophasic gels. J Eur Ceram Soc 26:2279–2284
8. Parmentier J, Vilminot S (1997) Influence of synthesis and composition of mullite crystallization. Chem Mater 9:1134–1137
9. Okada K, Aoki C, Ban T, Hayashi S, Yasumori A (1996) Effect of aging temperature on the structure of mullite precursor prepared from tetraethoxysilane and aluminium nitrate in ethanol solution. J Eur Ceram Soc 16:149–153
10. Kaya C, Butler EG, Lewis MH (2003) Microstructurally controlled mullite ceramics produced from monophasic and diphasic sol-derived pastes using extrusion. J Mater Sci 38:767–777
11. Bagchi B, Das S, Bhattacharya A, Basu R, Nandy P (2010) Mullite phase enhancement in Indian kaolins by addition of vanadium pentoxide. Appl Clay Sci 47:409–413
12. Hou P, Basu SN, Sarin VK (1999) Nucleation mechanisms in chemically vapour-deposited mullite coatings on SiC. J Mater Res 14:2952–2958
13. Dj Janackovic, Jokanovic V, Lj Kostic-Gvozdenovic, Uskokovic D (1998) Synthesis of mullite nanostructured spherical powder by ultrasonic spray pyrolysis. Nanostruct Mater 10:341–348
14. Song KC (1998) Preparation of mullitefibers from aluminium isopropoxide–aluminum nitrate–tetraethylorthosilicate solutions by sol–gel method. Mater Lett 35:290–296
15. Li J, Tong L, Wang X (2014) Preparation and mechanism of nano mullite powders from kaolin via open hydrothermal process. J Nanosci Nanotechnol 14:3876–3879
16. Ren L, Fu Z, Wang Y, Zhang F, Zhang J, Wang W, Wang H (2015) Fabrication of transparent mullite ceramic by spark plasma sintering from powders synthesized via sol–gel process combined with pulse current heating. Mater Des 83:753–759
17. Okada K, Yasohama S, Hayashi S, Yasumori A (1998) Sol–gel synthesis of mullite long fibres from water solvent systems. J Eur Ceram Soc 18:1879–1884
18. Cividanes LS, Campos TMB, Rodrigues LA, Brunelli DD, Thim GP (2010) Review of mullite synthesis routes by sol–gel method. J Sol-Gel Sci Technol 55:111–125
19. Schneider H, Saruhan B, Voll D, Merwin L, Sebald A (1993) Mullite precursor phases. J Eur Ceram Soc 11:87–94
20. Okada K (2008) Activation energy of mullitization from various starting materials. J Eur Ceram Soc 28:377–382
21. Tkalcec E, Kurajica S, Ivankovic H (2005) Diphasic aluminosilicate gels with two stage mullitizationin temperature range of 1200–1300 °C. J Eur Ceram Soc 25:613–626
22. Sundaresan S, Aksay IA (1991) Mullitization of diphasic aluminosilicate gels. J Am Ceram Soc 74:2388–2392
23. Zhou M, Sun K, Wu J (2001) Microstructures of mullite and mullite-alumina composite sintered from diphasic precursors. J Mater Sci Lett 20:2021–2023
24. Nishio T, Fujiki Y (1991) Preparation of mullite fiber by sol–gel method. J Ceram Soc Jpn 99:654–659
25. Ban T, Hayashi S, Yasumori A, Okada K (1996) Characterization of low temperature mullitization. J Eur Ceram Soc 16:127–132
26. Hong S-H, Messing GL (1997) Mullite transformation kinetics in P_2O_5−, TiO_2−, and B_2O_3− doped aluminosilicate gels. J Am Ceram Soc 80:1551–1559
27. Kong LB, Huang H, Zhang TS, Gan YB, Ma J, Boey F, Zhang RF (2003) Effect of transition metal oxides on mullite whisker formation from mechanochemically activated powders. Mater Sci Eng A 359:75–81
28. Kong LB, Chen YZ, Zhang TS, Ma J, Boey F, Huang H (2004) Effect of alkaline-earth oxides on phase formation and morphology development of mullite ceramics. Ceram Int 30:1319–1323
29. Martisius T, Giraitis R (2002) Influence of copper oxide on mullite formation from kaolinite. J Mater Chem 13:121–124
30. Bagchi B, Das S, Bhattacharya A, Basu R, Nandy P (2010) Effect of nickel and cobalt ions on low temperature synthesis of mullite by sol–gel technique. J Sol-Gel Sci Technol 55:135–141
31. Roy J, Bandyopadhyay N, Das S, Maitra S (2010) Role of V_2O_5 on the formation of chemical mullite from aluminosilicate precursor. Ceram Int 36:1603–1608
32. Bagchi B, Das S, Bhattacharya A, Basu R, Nandy P (2009) Nanocrystalline mullite synthesis at a low temperature: effect of copper ions. J Am Ceram Soc 92:748–751
33. Purushotham E, Gopi Krishna N (2013) X-ray determination of crystallite size and effect of lattice strain on Debye–Waller factors of platinum nano powders. Bull Mater Sci 36:973–976
34. Padmaja P, Anilkumar GM, Mukundan P, Aruldhas G, Warrier KGK (2001) Characterisation of stoichiometric sol–gel mullite by fourier transform infrared spectroscopy. Int J Inorg Mater 3:693–698
35. Kool A, Thakur P, Bagchi B, Rajak U, Das T, Kar S, Chakraborty G, Mukhopadhyay TK, Das S (2014) Effect of vanadic anhydride and copper oxide on the development of hard porcelain composite and its antibacterial activity. J Asian Ceram Soc 2:297–304
36. Ore'fice RL, Vasconselos WL (1997) Sol–gel transition and structural evolution on multicomponent gels derived from alumina silica system. J Sol-Gel Sci Technol 9:239–249
37. Schneider H, Komarneni S (2005) Mullite. Wiley-VCH, Weinheim
38. Treadwell DR, Dabbs DM, Aksay IA (1996) Mullite ($3Al_2O_3$–$2SiO_2$) synthesis with aluminosiloxanes. Chem Mater 8:2056–2060
39. Kool A, Thakur P, Bagchi B, Hoque NA, Das S (2015) Mechanical, dielectric and photoluminescence properties of alumina-mullite composite derived from natural Ganges clay. Appl Clay Sci 114:349–358
40. Heikes R, Johnston DR (1957) Mechanism of conduction in Li-substituted transition metal oxides. J Chem Phys 26:582–587
41. Kool A, Thakur P, Bagchi B, Hoque NA, Banerjee S, Das S (2015) Sol-gel synthesis of transition metal ion conjugated alumina-rich mullite nanocomposites with potential mechanical, dielectric and photoluminescence properties. RSC Adv 5:104299–104313